

Role of dipole-forbidden autoionizing resonances in nonresonant one-color two-photon single ionization of N₂

Kirk A. Larsen ^{1,2,*}, Roger Y. Bello ^{2,†}, Robert R. Lucchese,² Thomas N. Rescigno,² C. William McCurdy,^{2,3} Daniel S. Slaughter ² and Thorsten Weber ^{2,‡}

¹Graduate Group in Applied Science and Technology, University of California, Berkeley, California 94720, USA

²Chemical Sciences Division, Lawrence Berkeley National Laboratory, Berkeley, California 94720, USA

³Department of Chemistry, University of California, Davis, California 95616, USA



(Received 17 September 2020; accepted 1 December 2020; published 23 December 2020)

We present an experimental and theoretical energy- and angle-resolved study on the photoionization dynamics of nonresonant one-color two-photon single-valence ionization of neutral N₂ molecules. Using 9.3-eV photons produced via high-order harmonic generation and a three-dimensional momentum imaging spectrometer, we detect the photoelectrons and ions produced from one-color two-photon ionization in coincidence. Photoionization of N₂ populates the $X^2\Sigma_g^+$, $A^2\Pi_u$, and $B^2\Sigma_u^+$ ionic states of N₂⁺, where the photoelectron angular distributions associated with the $X^2\Sigma_g^+$ and $A^2\Pi_u$ states both vary with changes in photoelectron kinetic energy of only a few hundred meV. We attribute the rapid evolution in the photoelectron angular distributions to the excitation and decay of dipole-forbidden autoionizing resonances that belong to series of different symmetries, all of which are members of the Hopfield series, and compete with the direct two-photon single ionization.

DOI: [10.1103/PhysRevA.102.063118](https://doi.org/10.1103/PhysRevA.102.063118)

I. INTRODUCTION

The photoionization continuum of molecular nitrogen possesses both one- and two-electron resonances, i.e., shape resonances and autoionizing states, which can strongly influence the behavior of ejected photoelectrons. The observable that is most sensitive to these resonance effects is the energy-resolved photoelectron angular distribution (PAD). In the case of single-photon ionization these resonance effects have been studied extensively both experimentally and theoretically [1–15]. However, due to its complexity, nonresonant two-photon ionization has received far less attention, while it provides the opportunity to observe the effect of discrete continuum states on the angular distributions of the photoelectrons and ions that are symmetry- and/or parity-forbidden in single-photon excitation schemes [16]. Moreover, two-photon absorption resulting in single ionization is particularly sensitive to resonance and electron-electron correlation effects [17].

The presence of continuum-embedded discrete states can lead to interference effects, a paradigmatic example being the Fano resonance, where the scattering amplitudes of a resonant (discrete) and background (continuum) process interfere to give rise to the classic asymmetric line shape [18]. In photoionization, continuum states that decay via autoionization can provide an indirect channel to target states that can interfere with the direct ionization channel to those very same states [19–23]. This effect can be observed in PAD [20,24,25], where the amplitudes and phases of the angular momentum

components of the photoelectron scattering wave function from direct ionization interfere with those of the electron originating from autoionization.

The dipole oscillator strength of N₂ across most of the VUV photon energy range is quite weak, as the states that lie below ~12 eV are dipole-forbidden transitions, because of either spin conservation or parity conservation. Within the ionization continuum and below the $B^2\Sigma_u^+$ ionic state [situated at 18.74 eV in the Franck-Condon (FC) region] lies the Hopfield series of N₂ [26], a progression of narrow resonances emerging from continuum molecular Rydberg states converging to the $B^2\Sigma_u^+$ ionic state. Such quasibound states can decay through autoionization, where these two-electron resonances provide an indirect channel to the $X^2\Sigma_g^+$ and $A^2\Pi_u$ ionic states, along with the direct ionization channel to those very same target states. By choosing a suitable photon energy, these autoionizing states can thus be populated and studied via nonresonant one-color two-photon ionization.

In this work we present experimental and theoretical results on energy- and angle-resolved nonresonant one-color two-photon single ionization (NOTPSI) of molecular nitrogen using three-dimensional (3D) momentum imaging, where the photoelectron and the molecular cation are measured in coincidence. Using a 400-nm driving field, we produce and select VUV photons with an energy of 9.3 eV via high-order harmonic generation (HHG), which are then used to singly ionize the target via two-photon ionization. We observe that the energy-resolved PADs associated with the $X^2\Sigma_g^+$ and $A^2\Pi_u$ ionic states both vary appreciably with small changes in the photoelectron kinetic energy. We ascribe these effects to the excitation and decay of dipole-forbidden autoionizing resonances belonging to series possessing different total symmetries, which, in addition to the direct ionization channel, provide an indirect pathway to the target states.

*KLarsen@lbl.gov

†RYBelloromero@lbl.gov

‡TWeber@lbl.gov

II. EXPERIMENT

The valence photoionization dynamics in neutral N_2 was investigated using the cold target recoil ion momentum spectroscopy (COLTRIMS) technique [27–30], where the photoelectrons and cations produced by NOTPSI are collected with full 4π solid angle, and their 3D momenta are measured in coincidence on an event-by-event basis. The charged particles are guided by parallel DC electric and magnetic fields (11.34 V/cm, 4.0 G) towards position- and time-sensitive detectors at opposite ends of the 3D momentum imaging spectrometer. The detectors consist of a multichannel plate (MCP) stack in chevron configuration with a delay-line anode readout [31,32]. The electron and ion detectors are a three-layer hex-anode with a 80-mm MCP stack and a two layer quad-anode with a 120-mm MCP stack, respectively, where a charge carrier's 3D momentum is encoded into its hit position on the detector and its time-of-flight relative to the laser trigger. In this configuration, the energy resolution of the spectrometer for the electrons is roughly 1:10.

The laser system has been described previously [30], so we provide only a brief overview that emphasizes some recent modifications. Near-infrared (NIR) laser pulses (12 mJ, 45 fs, 800 nm) from a 50-Hz Ti:sapphire laser system are frequency doubled using a 0.25-mm-thick β -barium borate (BBO) crystal, where the copropagating NIR and blue fields are then separated using two dichroic mirrors. The reflected 400-nm photons (~ 3.6 mJ, ~ 50 fs) are used to generate femtosecond VUV pulses via HHG, by loosely focusing ($f = 6$ m) the 400-nm pulses into a 10-cm-long gas cell containing 2 Torr of krypton. The resulting VUV frequency comb is then separated from the 400-nm driving field by reflection from three Si mirrors near Brewster's angle for the blue light, resulting in a suppression of the driving field by a factor of $< 10^{-6}$. The 3rd harmonic (133 nm, 9.3 eV) is selected via transmission through a 0.25-mm-thick MgF_2 window, which totally suppresses the 5th harmonic and above and maintains the femtosecond pulse duration of the 3rd harmonic. The residual 400-nm pulses are also separated from the 3rd harmonic pulse temporally by roughly 700 fs, due to the difference in the group velocity dispersion (GVD) of the window at ω_0 and $3\omega_0$ [33,34]. After transmission through the window we estimate the pulse duration of the 3rd harmonic to be ~ 30 fs, based on its spectral bandwidth, its estimated attochirp, and the thickness and GVD of the MgF_2 window [35,36]. The femtosecond 9.3-eV pulses are then back-focused ($f = 15$ cm) into the 3D momentum imaging spectrometer using a protected Al mirror, the reflectance of which has been measured to be 43% at 9.3 eV [37]. The pulse energy of the 3rd harmonic on target is approximately 10 nJ, which was measured using a pair of broadband VUV filters (Acton Optics FB130-B-1D.3) and a calibrated photodiode. From our previous NOTPSI measurement of argon [17], the VUV spectrum of the 9.3-eV femtosecond pulse is known to be roughly Gaussian in shape and possesses no sidebands or pedestal, characteristic of the VUV frequency combs generated in the single-color high-order harmonic generation.

A rotationally and vibrationally cold beam of nitrogen molecules (approximately 80 K) is prepared via an adiabatic expansion through a 0.03-mm nozzle, which is then

collimated by a pair of skimmers. This molecular jet propagates perpendicular to the focused VUV beam, where the two intersect in the interaction region of the spectrometer ($\sim 0.01 \times 0.01 \times 0.20$ mm), resulting in NOTPSI of the target molecules at an average rate of ~ 0.3 events per VUV pulse.

III. THEORY

The potential energy curves of the neutral N_2 states relevant to this study were computed using the multireference configuration interaction (MRCI) capability of MOLPRO [38,39], with single and double excitations from an active space including four σ_g , four σ_u , two π_u , and two π_g orbitals, with the $1\sigma_g$ and $1\sigma_u$ core orbitals always doubly occupied. These orbitals were optimized using a state-averaged complete-active-space self-consistent field (CASSCF) calculation with one state of each symmetry, $^1\Sigma_g^+$, $^1\Pi_u$, $^1\Sigma_u^-$, and $^1\Delta_u$, included. The one-electron basis set was aug-cc-pVTZ [40,41], augmented by four s , four p , and four d Rydberg diffuse functions [42] centered at the bond midpoint.

One-photon ionization cross sections and photoelectron β parameters were calculated at a fixed internuclear distance of $R = 2.07$ a.u. using a multichannel configuration interaction method (MCCI) [43,44]. The scattering state at a fixed energy was represented on a single-center expanded grid, with a partial wave expansion up to $l_{\max} = 80$. The full N -electron scattering state was then written as a close-coupling expansion containing a sum of the products of $(N - 1)$ -electron ion state wave functions multiplied with one-electron photoelectron wave functions. The lowest eight ion states were included in the close-coupling expansion. The initial and ion states were computed performing a numerical CAS-CI using the orbitals from the CASSCF calculation discussed above. We considered as the intermediate state for ionization the $b^1\Pi_u$ ($2\sigma_u \rightarrow 1\pi_g$) valence state shown in Fig. 1, which is the first dipole allowed excited state of N_2 lying at ~ 13.5 eV above the ground state [45,46]. The three lowest ionization thresholds of N_2 were found to be ~ 15.6 , ~ 17.1 , and ~ 18.8 eV corresponding to ionization into the $X^2\Sigma_g^+$, $A^2\Pi_u$, and $B^2\Sigma_u^+$ N_2^+ ionic states, respectively.

Two-photon single ionization β_2 and β_4 anisotropy parameters have been calculated within the time-independent second-order perturbation theory framework [47–51]. For simplicity we have assumed a resonant transition to the $b^1\Pi_u$ excited state as the first photon absorption. Calculating the cross sections and anisotropy parameters for nonresonant two-photon single ionization of N_2 in lowest-order perturbation theory requires a sum of single-photon ionization amplitudes over a substantial number of intermediate states, which is beyond the scope of this study. The dipole couplings between the ground state and the intermediate state have been calculated using MOLPRO.

IV. RESULTS

The measured photoelectron energy spectrum is presented in Fig. 2(a), where we observe three peaks centered near 2.88, 1.63, and 0.15 eV, corresponding with the $X^2\Sigma_g^+$, $A^2\Pi_u$, and $B^2\Sigma_u^+$ ionic states of molecular nitrogen, respectively. The two-photon excitation energy and bandwidth are ~ 18.6 eV

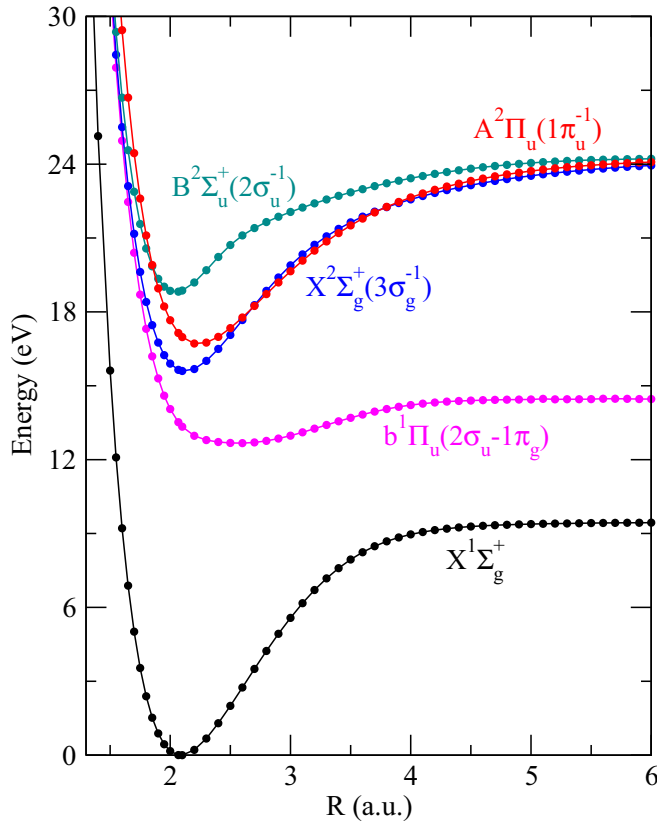


FIG. 1. Relevant potential energy curves of N_2 and N_2^+ . The figure shows the lowest $^1\Pi_u$ state of N_2 as well as the lowest three states of N_2^+ .

and ~ 300 meV, respectively. Hence, the measured linewidths of the three cationic states in Fig. 2(a) are largely determined by the spectral bandwidth of the VUV pulse, which exceeds the vibrational level spacing [see green (gray) vertical lines]. We point out that although our central two-photon energy lies below the ionization threshold of the $B^2\Sigma_u^+$ ionic state, the two-photon bandwidth of the excitation pulse enables its lowest vibrational level to be accessed. The $X^2\Sigma_g^+$ and $A^2\Pi_u$ state peaks are partitioned into two and three different photoelectron kinetic energy regions, respectively, for subsequent analysis. The horizontal black and red (gray) lines in Fig. 2(a) indicate the high- and low-energy regions, respectively, while the horizontal blue (dark gray) line indicates a middle-energy region that is considered in the case of the $A^2\Pi_u$ ionic state. The $X^2\Sigma_g^+$ state energy slices range from 2.50–2.85 and 2.85–3.20 eV, while the $A^2\Pi_u$ state slices span 1.18–1.64, 1.41–1.83, and 1.65–2.03 eV. These regions capture photoelectrons emerging from ionization events to different target state vibrational levels. The vertical green line segments in Fig. 2(a) indicate the energetic locations of the relevant vibrational levels of the $X^2\Sigma_g^+$ and $A^2\Pi_u$ ionic states and their corresponding FC factors [13]. In the $X^2\Sigma_g^+$ state, the high-energy region roughly corresponds with photoionization to the $\nu = 0$ level of the target, and the low-energy region captures photoionization to the $\nu = 1$ level. In the $A^2\Pi_u$ state, the high-energy slice roughly corresponds with populating the

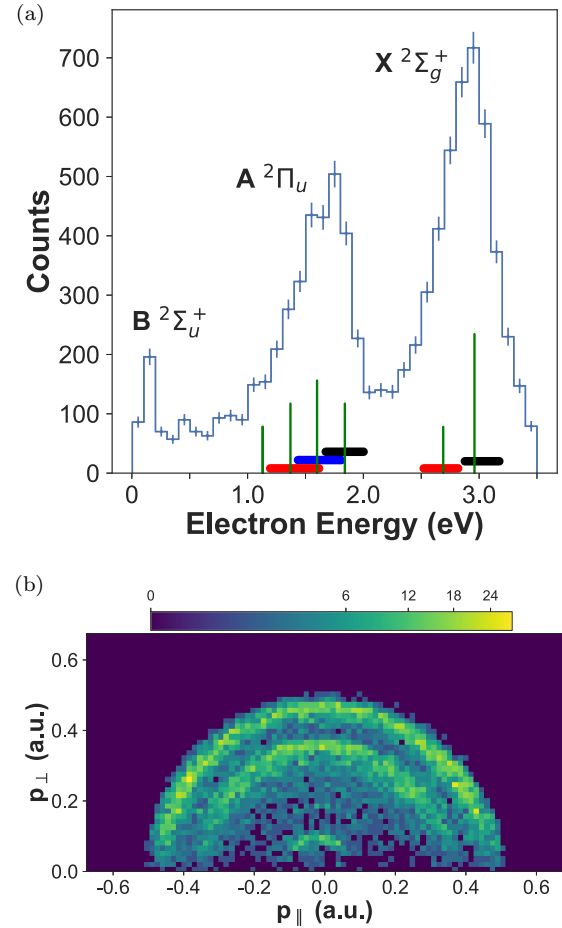


FIG. 2. (a) The measured photoelectron energy spectrum for NOTPSI of N_2 . The colored horizontal lines indicate different energy regions of the $X^2\Sigma_g^+$ and $A^2\Pi_u$ states that are subsequently analyzed. The vertical green lines roughly indicate the location of the relevant vibrational levels of the two ionic states and their corresponding one-photon oscillator strengths. (b) Photoelectron momentum distribution parallel and perpendicular to the VUV polarization.

$\nu = 0$ and 1 vibrational levels of the target, the middle-energy slice with the $\nu = 1, 2$, and 3 levels, and the low-energy slice with the $\nu = 2, 3$, and 4 levels. Most of these slices sum over two or three vibrational levels, as the two-photon bandwidth, energy resolution, and statistics do not permit a fully vibrationally resolved measurement.

The photoelectron momentum distributions for the transverse and parallel momentum components with respect to the VUV polarization vector for the three ionic states are shown in Fig. 2(b). Here we see three arcs of differing photoelectron momentum, corresponding to each of the three populated molecular ionic states. To gain more insight into the photoelectron emission pattern for each of these three ionic states, we turn to the angle-differential photoionization cross section.

For two-photon ionization processes, the energy-dependent angle-differential photoionization cross section of a target by

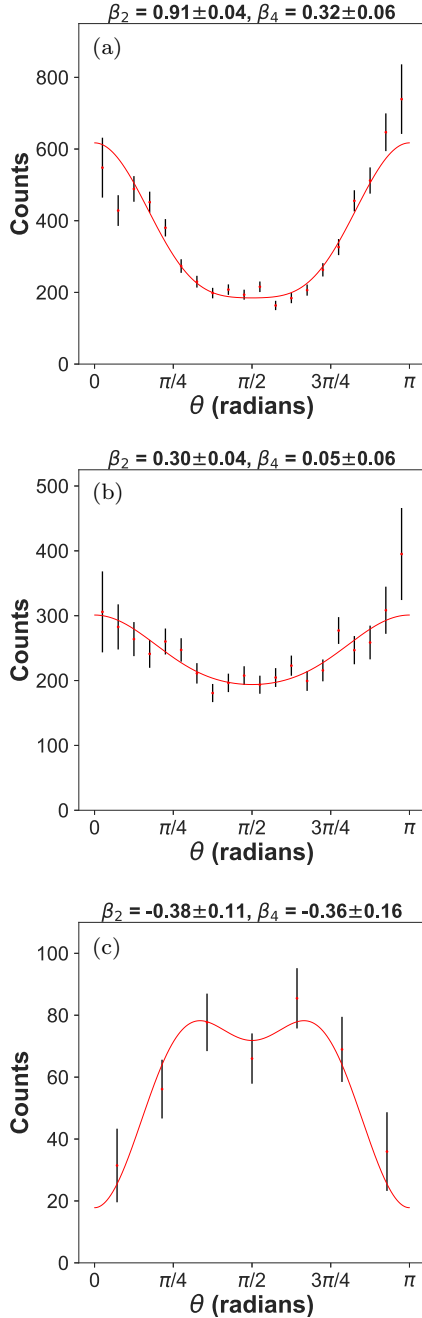


FIG. 3. The energy-integrated photoelectron angle-differential photoionization cross section for NOTPSI of N_2 to the first three ionic states: (a) the $X^2\Sigma_g^+$ state, (b) the $A^2\Pi_u$ state, and (c) the $B^2\Sigma_u^+$ state. The data were fitted using Eq. (1), and the retrieved β parameters are displayed above each plot.

linearly polarized light is given by

$$\frac{d^2\sigma}{d\Omega dE} = \frac{\sigma_0(E)}{4\pi} [1 + \beta_2(E)P_2(\cos\theta) + \beta_4(E)P_4(\cos\theta)], \quad (1)$$

where σ_0 is the total photoionization cross section, θ is the angle between the photoelectron momentum vector and the polarization vector of the light, E is the photoelectron kinetic energy, β_2 and β_4 are the second- and fourth-order anisotropy

TABLE I. The anisotropy (β) parameters retrieved from fitting the energy-integrated photoelectron angular distributions shown in Fig. 3 according to Eq. (1) for the $X^2\Sigma_g^+$, $A^2\Pi_u$, and $B^2\Sigma_u^+$ states of N_2^+ .

State	β_2	β_4
$X^2\Sigma_g^+$	0.91 ± 0.04	0.32 ± 0.06
$A^2\Pi_u$	0.30 ± 0.04	0.05 ± 0.06
$B^2\Sigma_u^+$	-0.38 ± 0.11	-0.36 ± 0.16

parameters, and P_2 and P_4 are the second- and fourth-order Legendre polynomials in the variable $\cos\theta$. The measured energy-integrated angle-differential photoionization amplitude for each of the $X^2\Sigma_g^+$, $A^2\Pi_u$, and $B^2\Sigma_u^+$ ionic states are presented in Figs. 3(a), 3(b), and 3(c), respectively. The data were fitted (solid red line) in accordance with Eq. (1), using the projection method discussed in Ref. [52], while the errors on the β parameters were determined via statistical bootstrapping [53].

The PADs associated with the $X^2\Sigma_g^+$ and $A^2\Pi_u$ ionic states depicted in Figs. 3(a) and 3(b) both exhibit peak intensity along the VUV polarization, more dramatically in the case of the $X^2\Sigma_g^+$ state, whereas the $A^2\Pi_u$ state PAD is more isotropic. The PAD associated with the $B^2\Sigma_u^+$ state in Fig. 3(c) appears bimodal in shape with two photoelectron emission peaks roughly perpendicular to the VUV field, each slightly offset to opposite sides of $\pi/2$. The energy-integrated β parameters associated with these three ionic states can all be found in Table I.

In Fig. 4 we show the energy-resolved PADs associated with the $X^2\Sigma_g^+$ ionic state, where we compare the low-photoelectron-energy portion with the high-energy portion, indicated by the red (gray) and black horizontal lines in Fig. 2(a). The energy-resolved β parameters for the $X^2\Sigma_g^+$ ionic state can be found in Table II. We find that the PADs vary between the two regions, where β_2 undergoes a slight decrease in value, while β_4 increases by more than a factor of 2, as the photoelectron kinetic energy increases. Here, the high-electron-energy PAD in Fig. 4(b) exhibits a minimum perpendicular to the VUV polarization vector broader than that of the low-energy PAD in Fig. 4(a).

In Fig. 5 we show the energy-resolved PADs associated with the $A^2\Pi_u$ ionic state, where we compare the low-, middle-, and high-energy regions, indicated by the red (gray), blue (dark gray), and black horizontal lines in Fig. 2(a), respectively. The energy-resolved β parameters associated

TABLE II. The anisotropy (β) parameters retrieved from fitting the energy-resolved photoelectron angular distributions according to Eq. (1) for the $X^2\Sigma_g^+$ and $A^2\Pi_u$ ionic states of N_2 , shown in Figs. 4 and 5.

State	Photoelectron energy (eV)	β_2	β_4
$X^2\Sigma_g^+$	2.50–2.85	0.98 ± 0.06	0.18 ± 0.09
	2.85–3.20	0.85 ± 0.05	0.42 ± 0.07
$A^2\Pi_u$	1.18–1.64	0.33 ± 0.06	-0.19 ± 0.08
	1.41–1.83	0.26 ± 0.05	0.04 ± 0.07
	1.65–2.03	0.25 ± 0.06	0.25 ± 0.08

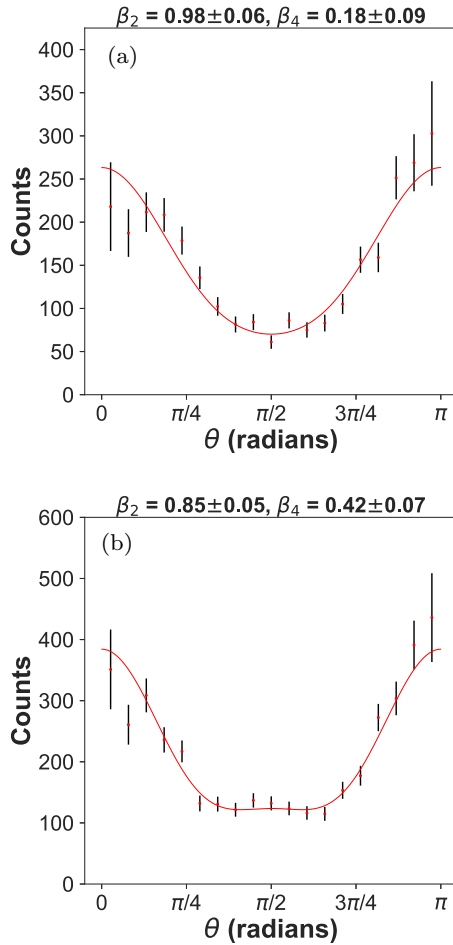


FIG. 4. The energy-resolved photoelectron angle-differential photoionization cross sections of N_2 following NOTPSI. Depicted is the photoelectron angular distribution for the $X^2\Sigma_g^+$ ionic state for two different energy regions in the photoelectron spectrum, indicated in Fig. 2, with the low-kinetic-energy region shown in panel (a) and the high-energy region in panel (b). The data were fitted using Eq. (1), and the retrieved β parameters are shown above each plot.

with the $A^2\Pi_u$ ionic state can be found in Table II. The PADs vary appreciably between the three slices, where β_2 slightly decreases in value, while β_4 increases in value dramatically and undergoes a sign change, as the photoelectron kinetic energy increases. The high-energy PAD in Fig. 5(c) exhibits maxima parallel to the ionizing field and a smaller peak perpendicular to the field, while the low-energy PAD in Fig. 5(a) shows a minimum perpendicular to the ionizing field and a smaller minimum parallel to the field. The middle-energy PAD in Fig. 5(b) resembles the energy-integrated PAD of Fig. 3(b), exhibiting a shallow minimum perpendicular to the VUV polarization vector.

For both states, the variation in the retrieved β_2 asymmetry parameter is not particularly significant, while the change in the β_4 parameter is more substantial. This is most striking in the $A^2\Pi_u$ state, where the value of β_4 changes sign, resulting in an appreciable variation in the PAD across the different photoelectron kinetic energy regions. Such a strong energy-dependent variation in the PAD is unlikely to stem from the effect of the final vibrational level on the scattering wave

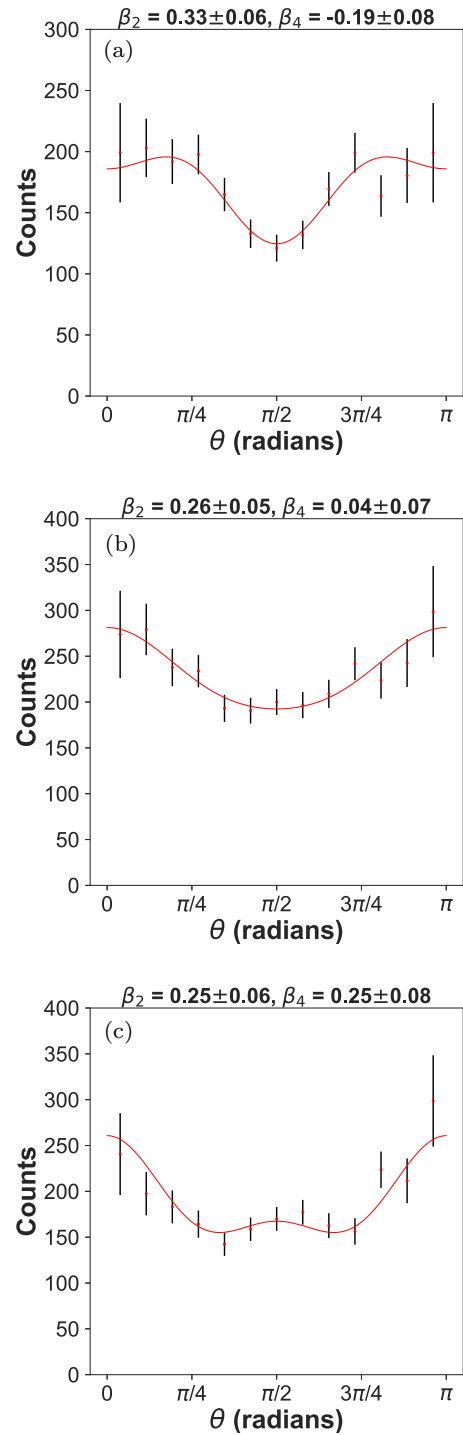


FIG. 5. The energy-resolved photoelectron angle-differential photoionization cross sections of N_2 following NOTPSI. Depicted is the photoelectron angular distribution for the $A^2\Pi_u$ ionic state for three different energy regions in the photoelectron spectrum, indicated in Fig. 2, with the low-kinetic-energy region shown in panel (a), the middle-energy region in panel (b), and the high-energy region in panel (c). The data were fitted using Eq. (1), and the retrieved β parameters are shown above each plot.

function, as the two-photon bandwidth exceeds the spacing of the vibrational levels in the cationic states, where the two-photon bandwidth is ~ 300 meV, while the level spacing in

the $A^2\Pi_u$ ionic state is ~ 230 meV [13]. Further, the different photoelectron energy regions considered here average over a family of adjacent vibrational levels, which should wash out the effect of the vibrational level on the photoelectron scattering wave function (i.e., our energy-resolved PADs integrate over numerous levels). Previous theoretical one-photon studies on the effect of the vibrational level of the target state of the photoelectron asymmetry parameter have indicated that the effect is negligible in the $A^2\Pi_u$ state [14], where we observe the strongest variation in the PAD. These effects are also unlikely to emerge from the shape resonance in the photoionization continuum of N_2 alone, as its peak in photoelectron kinetic energies (~ 32 eV) is much higher than that of the kinetic energies of the electrons corresponding to the populated continuum states in the present work.

In order to better understand the experimental findings, in particular, the rapid evolution in the measured PADs that are associated with the $A^2\Pi_u$ ionic state, we have performed one-photon single ionization calculations from a selected excited state of neutral N_2 . We chose the $b^1\Pi_u$ state, which is the lowest dipole-allowed electronic state lying ~ 13.5 eV above the N_2 ground state. The total one-photon ionization cross sections from the N_2 ($b^1\Pi_u$) state along with the corresponding photoelectron β parameters for the $^1\Sigma_g^+$, $^1\Pi_g$, and $^1\Delta_g$ dipole-allowed total symmetries are shown in Figs. 6, 7, and 8, respectively. All these symmetries have to be taken into account, as our experiment probes randomly oriented molecules, and the two-photon energy lies below the dissociative ionization threshold, preventing the molecular orientation at the instant of photoionization from being determined without prealignment. The cross sections were calculated at a single fixed nuclear geometry over an energy range between 17.4 and 18.7 eV, where the $X^2\Sigma_g^+$ and $A^2\Pi_u$ ionic states were accessible (see Fig. 1).

The photoionization cross section in each symmetry exhibits a collection of structures that can be attributed to the Hopfield series of autoionizing states converging to the $B^2\Sigma_u^+$ state of the ion. The Hopfield series has been previously studied, theoretically and experimentally, in the one-photon ionization from the N_2 ground state leading to $^1\Sigma_u^+$ and $^1\Pi_u$ final symmetries. In contrast, the corresponding photoionization cross sections from an excited state of N_2 have not been reported theoretically to the best of our knowledge. Two different series, np and nf , have been assigned in the cross sections using the Rydberg equation

$$E_n = V_{\text{ion}} - \frac{R}{(n - \delta)^2}, \quad (2)$$

where E_n represents the energy of the autoionizing state, V_{ion} is defined as the ionization potential, R is the Rydberg constant, n is the principal quantum number of the Rydberg electron, and δ is the quantum defect, which depends on the angular momentum l . For $l = 0$ a large quantum defect, i.e., $\delta \sim 1$, is expected, while δ decreases rapidly as l increases such that the nd and nf series ($l = 2$ and 3) are characterized by $\delta \sim 0$.

While the np and nf series coexist in the $^1\Sigma_g^+$ and $^1\Pi_g$ symmetries, seen in Figs. 6(a) and 7(a), only the nf is visible

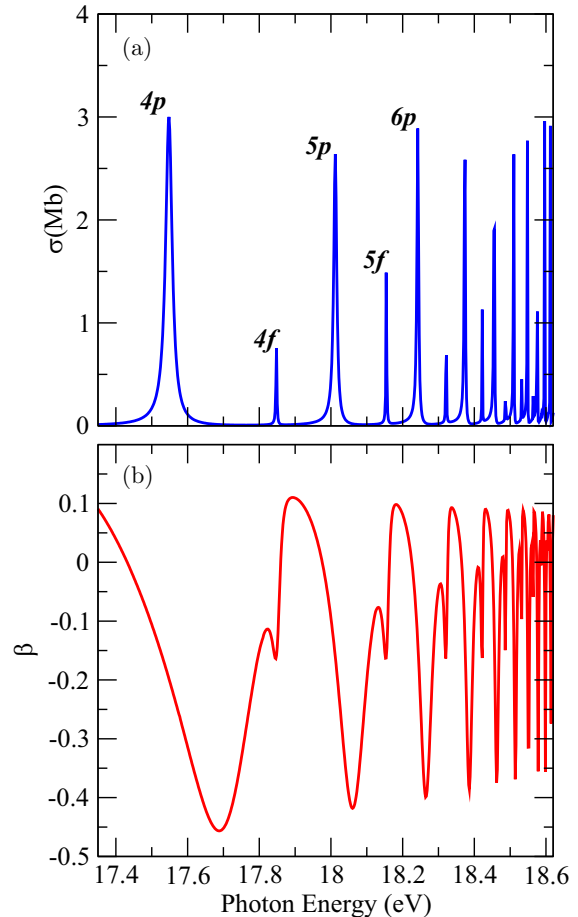


FIG. 6. (a) Total photoionization cross section from the N_2 ($b^1\Pi_u$) state between the second ($A^2\Pi_u$) and third ($B^2\Sigma_u^+$) ionization thresholds, while leaving the system in $^1\Sigma_g^+$ final symmetry. The nl labels indicate the $np\sigma_u$ and nf (δ_u or σ_u) series of the autoionizing states converging to the N_2^+ ($B^2\Sigma_u^+$) cation state. (b) Corresponding photoelectron asymmetry parameter for the one-photon transition. Note that the abscissa in this figure and in Figs. 7, 8, and 9 represents the energy of a two-photon transition from the ground state, where one photon is on resonance with the intermediate $b^1\Pi_u$ state, while the second photon energy is varied.

in the $^1\Delta_g$ symmetry, seen in Fig. 8(a). The np series, σ_u or π_u , are characterized by a slightly different quantum defect, $\delta \sim 0.56$ or $\delta \sim 0.66$, respectively, appearing thus at different energy positions. In contrast, the nf series presents the same quantum defect number $\delta \sim -0.002$ in each final symmetry. The effect of the autoionizing states on the PADs is highly significant. The β parameter dramatically changes as the photon energy crosses their energy position, seen in Figs. 6(b), 7(b), and 8(b). In addition, both series of autoionizing states generate completely different values of the β parameter. For instance, as observed in Fig. 7, the $5f$ autoionizing state gives rise to an asymmetry parameter of $\beta = 0.81$, while the $6p$ state is characterized by $\beta = 0.30$. It is important to mention that, although the magnitudes of the cross sections and β parameters depend on the initial state, the positions of these same series of autoionizing states do not change when a

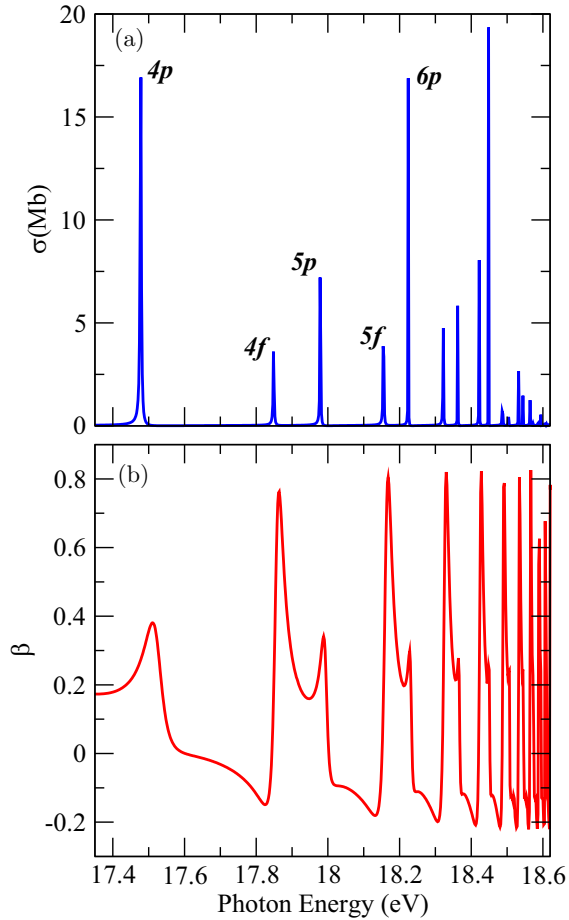


FIG. 7. As in Fig. 6 but leaving the system in $^1\Pi_g$ final symmetry. The nl labels indicate the $np\pi_u$ and nf (ϕ_u or π_u) series of the autoionizing states converging to the N_2^+ ($B^2\Sigma_u^+$) cation state.

different N_2 excited state is chosen as the initial state for the calculation.

An accurate calculation of the cross section for nonresonant two-photon single ionization of N_2 in lowest-order perturbation theory would require a sum of single-photon ionization amplitudes over a large number of ungerade intermediate electronic states, which is well beyond the scope of the present study. To simplify the calculation, while providing further insight into the experimental observations, we have performed two-photon ionization calculations using the neutral $b^1\Pi_u$ state as the single intermediate state. Figure 9 shows the calculated β_2 and β_4 parameters characterizing the two-photon ionization into the $A^2\Pi_u$ state of the ion. Both parameters exhibit strong variations as a function of the photon energy, as observed previously in Figs. 6, 7, and 8. This further underlines the effect of the autoionizing states on the PADs, as the autoionizing states appearing in each of the possible final symmetries are now taken into account. Considering the selected photoelectron kinetic energy intervals [see Fig. 2(a)], the np and nf Rydberg series contribute differently depending on the respective kinetic energy region, which results in completely different PADs as depicted in Figs. 5(a) to 5(c). The finite bandwidths of the VUV pulses used in the present experiments produce photoelectrons from

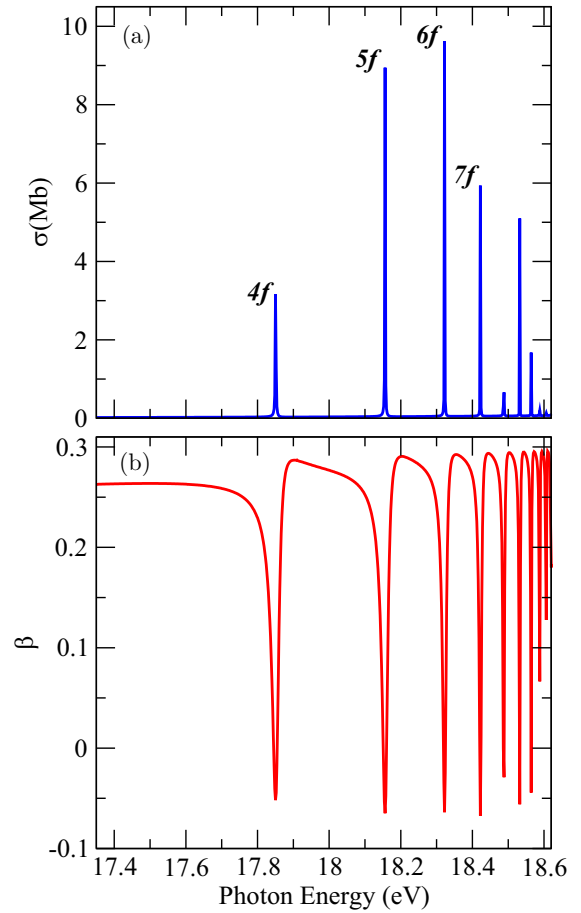


FIG. 8. As in Fig. 6 but leaving the system in $^1\Delta_g$ final symmetry. The nl labels indicate the nf (δ_u or σ_u) series of the autoionizing states converging to the N_2^+ ($B^2\Sigma_u^+$) cation state.

several final ion vibrational levels. It has also been shown in previous vibrationally resolved single-channel calculations, which do not treat autoionization processes [14], that the influence of vibrational levels of the final state on the anisotropy parameter for the $A^2\Pi_u$ state is negligible. This prediction is consistent with the present calculations, stressing the major role of the continuum autoionizing states in NOTPSI of N_2 , which manifests in a rapid variation in the anisotropy parameters. Going beyond the scope of the present work, a quantitative comparison between the theoretical and experimental PADs would, however, require further calculations that take into account the nonresonant character of the first photon absorption step. This implies including dipole couplings between the ground state and several excited intermediate states as well as incorporating continuum-continuum dipole couplings.

V. CONCLUSION

We have presented energy- and angle-resolved experimental and theoretical results on the photoionization dynamics of N_2 , analyzing ionic-state-selective photoelectron angular distribution following NOTPSI of neutral nitrogen molecules using coincidence 3D momentum imaging and intense 9.3-eV femtosecond pulses produced via 400-nm driven HHG. Two-

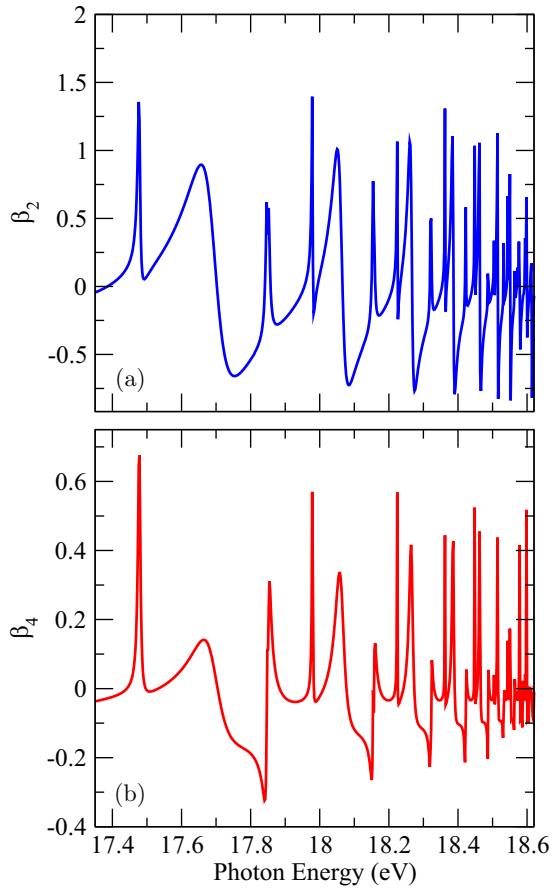


FIG. 9. Two-photon photoelectron asymmetry parameters, β_2 (a) and β_4 (b), correlated to the $A^2\Pi_u$ state of the N_2^+ ion.

photon single ionization populates the first three ionic states of the molecular nitrogen cation, where we find that the PADs associated with the $X^2\Sigma_g^+$ and $A^2\Pi_u$ ionic states of N_2^+ both vary with minor changes in the photoelectron kinetic energy. We attribute this strong variation in the electron emission patterns on the photoelectron energy to the excitation and decay of dipole-forbidden autoionizing resonances of different total symmetry that belong to the Hopfield series. In addition to the direct ionization channel, these continuum-embedded discrete states provide an indirect pathway to the $X^2\Sigma_g^+$ and $A^2\Pi_u$ final states. The 9.3-eV photon energy used in the present experiment can be very slightly detuned using plasma blueshifting of the harmonics; however, this effect is small and limited in range. This unfortunately prevented a careful and thorough exploration of the effect of the photon energy on the photoionization dynamics in the current exper-

imental setup. However, a more tunable VUV light source, such as a monochromatized VUV free-electron laser, could allow the photon energy to be scanned and the effect of intermediate resonances to be explored in more detail in the future.

Despite our limited theoretical treatment, only invoking a single intermediate state and hence treating the two-photon ionization as resonant, our calculations provide insight into the nonresonant two-photon ionization dynamics, highlighting the important role of the dipole-forbidden autoionizing states in shaping the PADs and resulting β parameters. Further calculations involving a larger number of intermediate states are beyond the scope of this work; however, the computed energies of the dipole-forbidden autoionizing states are insensitive to the intermediate state chosen, which suggests that such autoionizing resonances will remain important in the nonresonant regime.

The two competing pathways of autoionization and direct ionization can interfere for electrons ionized to the same final state. Experiments sensitive to such interference phenomena require the energy and the angular momentum of detected autoionization electrons and photoelectrons (corresponding to indirect and direct pathways, respectively) to be identical. As the electron in the continuum can share angular momentum with the molecular axis in several ways, interference can only be observed for fixed-in-space molecular N_2^+ cations. As mentioned before, in the present work the target N_2 molecules were randomly orientated, and hence we could not isolate the small subset of events that would sensitively exhibit interference effects in the PADs. Future experiments could employ a multicolor interrogation scheme that would enable prealigning the molecular axis via an additional laser pulse, which would be able to impulsively align the neutral molecule with respect to the polarization vector of the intense VUV beam prior to ionization. The necessary degree of alignment to achieve molecular orientations where the final total wave function for the two ionization pathways will be indistinguishable is hereby expected to depend on the density of states of the selected target molecule.

ACKNOWLEDGMENTS

Work at LBNL was supported by the U.S. Department of Energy Office of Basic Energy Sciences, Division of Chemical Sciences, Biosciences, and Geosciences under Contract No. DE-AC02-05CH11231, and used resources of the National Energy Research Computing Center, a U.S. Department of Energy (U.S. DOE) Office of Science User Facility supported by the Office of Science of the DOE, and the Lawrence computational cluster resource provided by the IT Division at the Lawrence Berkeley National Laboratory.

- [1] B. Basden and R. R. Lucchese, Vibrationally resolved cross sections, and asymmetry parameters for the photoionization of N_2 with coupling between the $(3\sigma_g)^{-1}$ and the $(2\sigma_u)^{-1}$ channels, *Phys. Rev. A* **37**, 89 (1988).
- [2] R. E. Stratmann, G. Bandarage, and R. R. Lucchese, Electron-correlation effects in the photoionization of N_2 , *Phys. Rev. A* **51**, 3756 (1995).

- [3] R. R. Lucchese, G. Raseev, and V. McKoy, Studies of differential and total photoionization cross sections of molecular nitrogen, *Phys. Rev. A* **25**, 2572 (1982).
- [4] R. R. Lucchese and R. W. Zurales, Comparison of the random-phase approximation with the multichannel frozen-core Hartree-Fock approximation for the photoionization of N_2 , *Phys. Rev. A* **44**, 291 (1991).

- [5] M. Ilchen, S. Deinert, L. Glaser, F. Scholz, J. Seltmann, P. Walter, and J. Viefhaus, Photoelectron angular distribution studies of the outer valence states of N_2 , *J. Phys. B* **45**, 225102 (2012).
- [6] E. W. Plummer, T. Gustafsson, W. Gudat, and D. E. Eastman, Partial photoionization cross sections of N_2 and CO using synchrotron radiation, *Phys. Rev. A* **15**, 2339 (1977).
- [7] S. H. Southworth, A. C. Parr, J. E. Hardis, and J. L. Dehmer, Channel coupling and shape resonance effects in the photoelectron angular distributions of the $3\sigma_g^{-1}$ and $2\sigma_u^{-1}$ channels of N_2 , *Phys. Rev. A* **33**, 1020 (1986).
- [8] A. C. Parr, D. L. Ederer, B. E. Cole, J. B. West, R. Stockbauer, K. Codling, and J. L. Dehmer, Triply-Differential Photoelectron Studies of Molecular Autoionization Profiles: The 710–730 Å Region of the N_2 Spectrum, *Phys. Rev. Lett.* **46**, 22 (1981).
- [9] M. Raoult, H. L. Rouzo, G. Raseev, and H. Lefebvre-Brion, *Ab initio* approach to the multichannel quantum defect calculation of the electronic autoionisation in the Hopfield series of N_2 , *J. Phys. B* **16**, 4601 (1983).
- [10] M. Ogawa and Y. Tanaka, Rydberg absorption series of N_2 , *Can. J. Phys.* **40**, 1593 (1962).
- [11] K. P. Huber, G. Stark, and K. Ito, Rotational structure in the Hopfield series of N_2 , *J. Chem. Phys.* **98**, 4471 (1993).
- [12] M. Klinker, C. Marante, L. Argenti, J. González-Vázquez, and F. Martín, Electron correlation in the ionization continuum of molecules: Photoionization of N_2 in the vicinity of the Hopfield series of autoionizing states, *J. Phys. Chem. Lett.* **9**, 756 (2018).
- [13] A. J. Yench, K. Ellis, and G. C. King, High-resolution threshold photoelectron and photoion spectroscopy of molecular nitrogen in the 15.0–52.7 eV photon energy range, *J. Electron Spectrosc. Relat. Phenom.* **195**, 160 (2014).
- [14] E. Plésiat, P. Decleva, and F. Martín, Vibrationally resolved photoelectron angular distributions from randomly oriented and fixed-in-space N_2 and CO molecules, *J. Phys. B* **45**, 194008 (2012).
- [15] E. Plésiat, P. Decleva, and F. Martín, Vibrational branching ratios in the photoelectron spectra of N_2 and CO: Interference and diffraction effects, *Phys. Chem. Chem. Phys.* **14**, 10853 (2012).
- [16] K. A. Larsen, R. R. Lucchese, D. S. Slaughter, and T. Weber, Distinguishing resonance symmetries with energy-resolved photoion angular distributions from ion-pair formation in O_2 following two-photon absorption of a 9.3 eV femtosecond pulse, *J. Chem. Phys.* **153**, 021103 (2020).
- [17] K. A. Larsen, D. S. Slaughter, and T. Weber, Angle-resolved nonresonant two-photon single ionization of argon using 9.3-eV photons produced via high-order harmonic generation, *Phys. Rev. A* **101**, 061402(R) (2020).
- [18] U. Fano, Effects of configuration interaction on intensities and phase shifts, *Phys. Rev.* **124**, 1866 (1961).
- [19] R. Y. Bello, S. E. Canton, D. Jelovina, J. D. Bozek, B. Rude, O. Smirnova, M. Y. Ivanov, A. Palacios, and F. Martin, Reconstruction of the time-dependent electronic wave packet arising from molecular autoionization, *Sci. Adv.* **4**, eaat3962 (2018).
- [20] M. Eckstein, C.-H. Yang, F. Frassetto, L. Poletto, G. Sansone, M. J. J. Vrakking, and O. Kornilov, Direct Imaging of Transient Fano Resonances in N_2 Using Time-, Energy-, and Angular-Resolved Photoelectron Spectroscopy, *Phys. Rev. Lett.* **116**, 163003 (2016).
- [21] A. Kaldun, A. Blättermann, V. Stooß, S. Donsa, H. Wei, R. Pazourek, S. Nagele, C. Ott, C. D. Lin, J. Burgdörfer, and T. Pfeifer, Observing the ultrafast buildup of a Fano resonance in the time domain, *Science* **354**, 738 (2016).
- [22] G. Sansone, F. Kelkensberg, J. F. Pérez-Torres, F. Morales, M. F. Kling, W. Siu, O. Ghafur, P. Johnsson, M. Swoboda, E. Benedetti *et al.*, Electron localization following attosecond molecular photoionization, *Nature (London)* **465**, 763 (2010).
- [23] H. Wang, M. Chini, S. Chen, Chang-H. Zhang, F. He, Y. Cheng, Y. Wu, U. Thumm, and Z. Chang, Attosecond Time-Resolved Autoionization of Argon, *Phys. Rev. Lett.* **105**, 143002 (2010).
- [24] P. O’Keeffe, P. Bolognesi, A. Moise, R. Richter, Y. Ovcharenko, and L. Avaldi, Vibrationally resolved photoionization of N_2 near threshold, *J. Chem. Phys.* **136**, 104307 (2012).
- [25] F. Martín, J. Fernández, T. Havermeier, L. Foucar, Th. Weber, K. Kreidi, M. Schöffler, L. Schmidt, T. Jahnke, O. Jagutzki, A. Czasch, E. P. Benis, T. Osipov, A. L. Landers, A. Belkacem, M. H. Prior, H. Schmidt-Böcking, C. L. Cocke, and R. Dörner, Single photon-induced symmetry breaking of H_2 dissociation, *Science* **315**, 629 (2007).
- [26] J. J. Hopfield, Absorption and emission spectra in the region $\lambda 600-1100$, *Phys. Rev.* **35**, 1133 (1930).
- [27] R. Dörner, V. Mergel, O. Jagutzki, L. Spielberger, J. Ullrich, R. Moshhammer, and H. Schmidt-Böcking, Cold target recoil ion momentum spectroscopy: A ‘momentum microscope’ to view atomic collision dynamics, *Phys. Rep.* **330**, 95 (2000).
- [28] J. Ullrich, R. Moshhammer, A. Dorn, R. Dörner, L. Ph. H. Schmidt, and H. Schmidt-Böcking, Recoil-ion and electron momentum spectroscopy: Reaction-microscopes, *Rep. Prog. Phys.* **66**, 1463 (2003).
- [29] T. Jahnke, T. Weber, T. Osipov, A. L. Landers, O. Jagutzki, L. Ph. H. Schmidt, C. L. Cocke, M. H. Prior, H. Schmidt-Böcking, and R. Dörner, Multicoincidence studies of photo and Auger electrons from fixed-in-space molecules using the COLTRIMS technique, *J. Electron Spectrosc. Relat. Phenom.* **141**, 229 (2004).
- [30] F. P. Sturm, T. W. Wright, D. Ray, I. Zalyubovskaya, N. Shivaram, D. S. Slaughter, P. Ranitovic, A. Belkacem, and T. Weber, Time resolved 3D momentum imaging of ultrafast dynamics by coherent VUV-XUV radiation, *Rev. Sci. Instrum.* **87**, 063110 (2016).
- [31] Roentdek, Roentdek delayline detectors.
- [32] O. Jagutzki, A. Cerezo, A. Czasch, R. Dorner, M. Hattas, M. Huang, V. Mergel, U. Spillmann, K. Ullmann-Pfleger, T. Weber *et al.*, Multiple hit readout of a microchannel plate detector with a three-layer delay-line anode, *IEEE Trans. Nucl. Sci.* **49**, 2477 (2002).
- [33] T. K. Allison, J. van Tilborg, T. W. Wright, M. P. Hertlein, R. W. Falcone, and A. Belkacem, Separation of high order harmonics with fluoride windows, *Opt. Express* **17**, 8941 (2009).
- [34] H. H. Li, Refractive index of alkaline earth halides and its wavelength and temperature derivatives, *J. Phys. Chem. Ref. Data* **9**, 161 (1980).
- [35] T. Sekikawa, T. Katsura, S. Miura, and S. Watanabe, Measurement of the Intensity-Dependent Atomic Dipole Phase of a High Harmonic by Frequency-Resolved Optical Gating, *Phys. Rev. Lett.* **88**, 193902 (2002).
- [36] T. Sekikawa, T. Ohno, T. Yamazaki, Y. Nabekawa, and S. Watanabe, Pulse Compression of a High-Order Harmonic by

- Compensating the Atomic Dipole Phase, *Phys. Rev. Lett.* **83**, 2564 (1999).
- [37] K. A. Larsen, J. P. Cryan, N. Shivaram, E. G. Champenois, T. W. Wright, D. Ray, O. Kostko, M. Ahmed, A. Belkacem, and D. S. Slaughter, VUV and XUV reflectance of optically coated mirrors for selection of high harmonics, *Opt. Express* **24**, 18209 (2016).
- [38] H.-J. Werner, P. J. Knowles, G. Knizia, F. R. Manby, and M. Schütz, Molpro: A general-purpose quantum chemistry program package, *WIREs Comput. Mol. Sci.* **2**, 242 (2012).
- [39] H.-J. Werner, P. J. Knowles, G. Knizia, F. R. Manby, M. Schütz, P. Celani, T. Korona, R. Lindh, A. Mitrushenkov, G. Rauhut, K. R. Shamasundar, T. B. Adler, R. D. Amos, A. Bernhardsson, A. Berning, D. L. Cooper, M. J. O. Deegan, A. J. Dobbyn, F. Eckert, E. Goll *et al.*, MOLPRO, version 2015.1, a package of *ab initio* programs, 2015.
- [40] T. H. Dunning, Gaussian basis sets for use in correlated molecular calculations. I. The atoms boron through neon and hydrogen, *J. Chem. Phys.* **90**, 1007 (1989).
- [41] R. A. Kendall, T. H. Dunning, and R. J. Harrison, Electron affinities of the first-row atoms revisited: Systematic basis sets and wave functions, *J. Chem. Phys.* **96**, 6796 (1992).
- [42] K. Kaufmann, W. Baumeister, and M. Jungen, Universal Gaussian basis sets for an optimum representation of Rydberg and continuum wavefunctions, *J. Phys. B* **22**, 2223 (1989).
- [43] R. E. Stratmann and R. R. Lucchese, A graphical unitary group approach to study multiplet specific multichannel electron correlation effects in the photoionization of O₂, *J. Chem. Phys.* **102**, 8493 (1995).
- [44] R. E. Stratmann, R. W. Zureski, and R. R. Lucchese, Multiplet-specific multichannel electron-correlation effects in the photoionization of NO, *J. Chem. Phys.* **104**, 8989 (1996).
- [45] W. F. Chan, G. Cooper, R. N. S. Sodhi, and C. E. Brion, Absolute optical oscillator strengths for discrete and continuum photoabsorption of molecular nitrogen (11–200 eV), *Chem. Phys.* **170**, 81 (1993).
- [46] K. Dressler, The lowest valence and Rydberg states in the dipole-allowed absorption spectrum of nitrogen. A survey of their interactions, *Can. J. Phys.* **47**, 547 (1969).
- [47] R. N. Dixon, Recoil anisotropy following multiphoton dissociation via near-resonant intermediate states, *J. Chem. Phys.* **122**, 194302 (2005).
- [48] R. N. Dixon, J. M. Bayley, and M. N. R. Ashfold, The rotational structure of three-photon resonances of polyatomic molecules, *Chem. Phys.* **84**, 21 (1984).
- [49] G. C. Nieman, Vibronic intensities and rotational line strength factors for the three-photon absorption spectrum of ammonia, *J. Chem. Phys.* **75**, 584 (1981).
- [50] R. G. Bray and R. M. Hochstrasser, Two-photon absorption by rotating diatomic molecules, *Mol. Phys.* **31**, 1199 (1976).
- [51] D. L. Andrews, The theory of double-beam three-photon absorption, *J. Chem. Phys.* **77**, 2831 (1982).
- [52] X.-J. Liu, R. R. Lucchese, A. N. Grum-Grzhimailo, Y. Morishita, N. Saito, G. Prümper, and K. Ueda, Molecular-frame photoelectron and electron-frame photoion angular distributions and their interrelation, *J. Phys. B* **40**, 485 (2007).
- [53] B. Efron, Bootstrap methods: Another look at the jackknife, in *Breakthroughs in Statistics*, Springer Series in Statistics, edited by S. Kotz and N. L. Johnson (Springer, New York, 1992), pp. 569–593.